ACS NANO
Cite This: ACS Nano 2018, 12, 3541−3550
www.acsnano.org

ARTICLE

Templated Assembly of a Functional Ordered Protein Macromolecular Framework from P22 Virus-like Particles

Kimberly McCoy,[†] Masaki Uchida,[†] Byeongdu Lee,[‡] and Trevor Douglas*[,†]

[†]Department of Chemistry, Indiana University, 800 East Kirkwood Avenue, Bloomington, Indiana 47405, United States

[‡]X-ray Science Division, Advanced Photon Source, Argonne National Laboratory, 9700 South Cass Avenue, Argonne, Illinois 60439, United States

Supporting Information

ABSTRACT: **Bottom-up construction of mesoscale materials using biologically derived nanoscale building blocks enables engineering of desired physical properties using green production methods. Virus-like particles (VLPs) are exceptional building blocks due to their monodispersed sizes, geometric shapes, production ease, proteinaceous composition, and our ability to independently functionalize the interior and exterior interfaces. Here a VLP, derived from bacteriophage P22, is used as a building block for the fabrication of a protein macromolecular framework (PMF), a tightly linked 3D network of functional protein cages that exhibit long-range order and catalytic activity. Assembly of PMFs was electrostatically templated, using amine-terminated dendrimers, then locked into place with a ditopic cementing protein that binds to P22. Long-range order is preserved on removal of the dendrimer, leaving a framework material composed completely of protein. Encapsulation of β-glucosidase enzymes inside of P22 VLPs results in formation of stable, condensed-phase materials with high local concentration of enzymes generating catalytically active PMFs.**

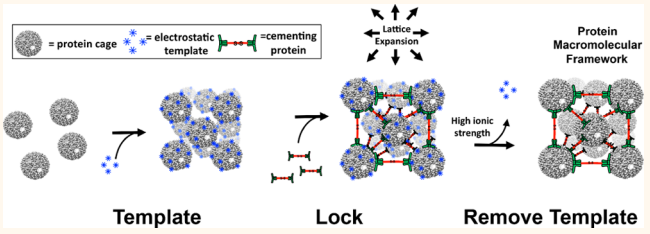

KEYWORDS: *self-assembly, virus-like particle (VLP), decoration protein, catalytic material, protein framework, templated assembly, nanoreactor*

Self-assembly of nanoscale building blocks to form geometrically controlled molecular frameworks is of great interest for creating functional porous materials.[1−3] Metal−organic frameworks (MOFs), composed of metal nodes coordinated to multidentate organic linkers,[4] exhibit a wide range of functionality dictated by the arrangement and composition of their molecular building blocks and have been studied for their use in gas storage,[5] heterogeneous catalysis,[6] and separation.[7,8] The systematic approach of creating design rules for MOF synthesis to create materials with specific structure and function has led to the rapid increase in useful MOF materials.[9] Biomolecular building blocks have been incorporated as the organic components of MOFs, and the resulting materials exhibit a range of structural, chemical, and catalytic diversity.[10−13] Additionally, biomolecule-based frameworks have been created using polymers[14] and nanoparticles[15,16] as linkage motifs.

The use of proteins in particular for the generation of framework materials is an exciting direction for nanomaterial development, as these molecules can be biologically synthesized and genetically or chemically modified, often without sacrificing structure or function,[17] to generate programmed building blocks that can self-assemble into higher ordered structures.[18] Because of the wide range of programmable intermolecular interactions available, protein-based molecular frameworks can be finely tuned to control their properties. Although less prevalent that MOFs, examples of protein-based molecular frameworks are emerging and include protein crystals that have been created not for structure elucidation but as a scaffold to selectively confine and store enzymes[19] as well as crystalline protein assemblies, which exhibit controlled porosity.[20,21] Here we describe the formation of a protein macromolecular framework (PMF), which is conceptually analogous to a MOF but is composed only of protein cages, derived from a virus, and protein linkers.

Virus-like particles (VLPs), self-assembled from multiple copies of subunit proteins into defined cage-like structures, are exemplary building blocks for materials construction because of their highly symmetric structures and ability to self-assemble from minimal protein building blocks into highly mono-

Received: January 19, 2018
Accepted: March 20, 2018
Published: March 20, 2018

DOI: 10.1021/acsnano.8b00528
ACS Nano 2018, 12, 3541−3550

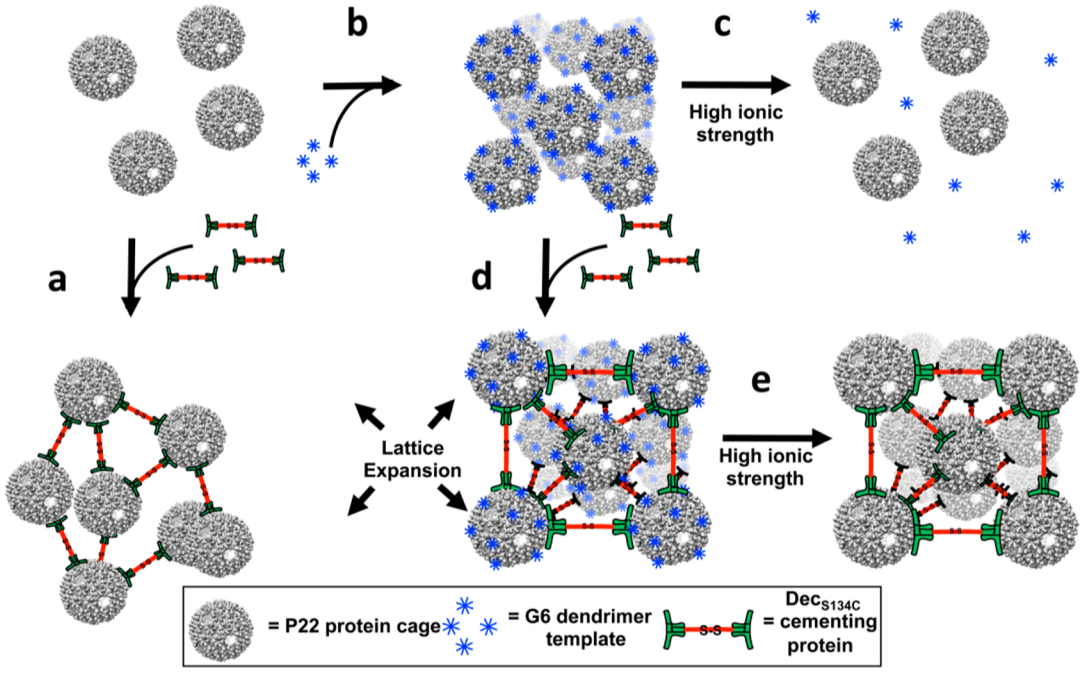

Figure 1. Idealized cartoon depicting the concept of protein macromolecular framework formation. Negatively charged P22$_{E2}$ virus-like particles are mixed with either (a) Dec$_{S134C}$ cementing proteins or (b) positively charged PAMAM generation 6 dendrimers (G6) to yield an amorphous array or an ordered array, respectively. When ionic strength is increased, (c) the array disassembles. (d) Dec$_{S134C}$ cementing proteins are added to G6 templated arrays to lock the structure in place while concomitantly increasing the lattice parameter approximately 3 nm. (e) Ionic strength is then increased, removing the G6 template but preserving the structure, yielding a protein macromolecular framework. (The number of Dec$_{S134C}$ bound to P22 is significantly higher in samples. It is depicted here as a lower amount for visual simplicity).

dispersed particles that can entrap desired cargo molecules.[22] VLPs have also been assembled into layers or three-dimensional architectures, thus offering the potential to fabricate structures at larger length scales.[3,23−25] The P22 VLP, derived from bacteriophage P22, is a 56 nm icosahedron, which self-assembles from 420 copies of a coat protein (CP) and 100−300 copies of an internalized scaffolding protein (SP).[26] P22 can be produced in large quantities and is highly tolerant to genetic and chemical modifications.[27,28] Through genetic fusion of cargo proteins to the SP, P22 can be directed to encapsulate many copies of the protein cargo without affecting capsid morphology.[29−33] Additionally, P22 VLPs can be obtained in three distinct morphologies: procapsid (PC), the initial assembly product of CP and SP; expanded (EX), which is larger in diameter by 8 nm and more angular; and wiffleball (WB), which is structurally similar to the EX form but missing 12 pentamers from the icosahedron, resulting in 10 nm pores.[34−36] The modularity of P22, where size, morphology, internal cargo, and external surface characteristics can be independently modified, make it a versatile building block for the construction of functional, well-defined condensed-phase materials as well as PMFs. In this work we construct PMFs using a variant of the P22 CP, P22$_{E2}$, exhibiting a small peptide ((VAALEKE)$_2$) at the surface-exposed C-terminus, which introduces repulsive interparticle interactions, allowing the formation of more ordered structures.[37,38]

In addition, a homotrimeric capsid decoration protein (Dec) has been shown to bind the exterior of the EX and WB morphologies of P22 as well as matured P22 virions in a site-specific manner.[39] Upon binding, the C-termini of Dec are directed away from the capsid surface.[40] We have previously shown that binding Dec or modified Dec to P22 is a powerful tool that allows for capsid stabilization[41] as well as exterior molecular presentation, since proteins can be expressed as Dec−cargo fusions.[42] There are 80 Dec binding sites on P22, 60 tight binding sites located at the quasi 3-fold axes nearest the icosahedral 2-fold axes, and 20 weaker binding sites at the true 3-fold axes.[40] We have previously shown that modification of the C-terminus of Dec, in which a terminal cysteine residue is displayed (Dec$_{S134C}$), results in formation of a head-to-head dimer of the trimeric protein upon oxidation, enabling Dec$_{S134C}$ to act as a ditopic linker between P22 EX capsids.[43] Due to the fast and almost irreversible binding of Dec to the P22 capsid and the high degree of multivalency, mixing ditopic Dec$_{S134C}$ with P22 results in a highly cross-linked protein material, but which lacks any long-range order.

Here, inspired by work showing the controlled assembly of protein cages using dendrimers,[44,45] we describe the formation and characterization of a protein macromolecular framework, an ordered 3D array of P22 VLPs connected by symmetry-specific protein linkers. P22$_{E2}$ VLPs are first electrostatically templated into an ordered array using amine-terminated generation 6 poly(amidoamine) dendrimers (G6) and then cemented into place *via* addition of the ditopic capsid decoration protein Dec$_{S134C}$ (Figure 1).

Upon removal of G6 under high ionic strength conditions, the resultant material retained the ordered face-centered cubic lattice structure but exhibited an increased interparticle spacing and associated expanded lattice parameter. PMFs constructed from P22$_{E2}$ capsids encapsulating multiple copies of a *β*-glucosidase enzyme impart catalytic activity to the material, which can be easily recovered after catalysis and thus recycled. PMFs also remain assembled and catalytically active after heating, freezing, and drying, demonstrating the stability of

DOI: 10.1021/acsnano.8b00528
ACS Nano 2018, 12, 3541−3550

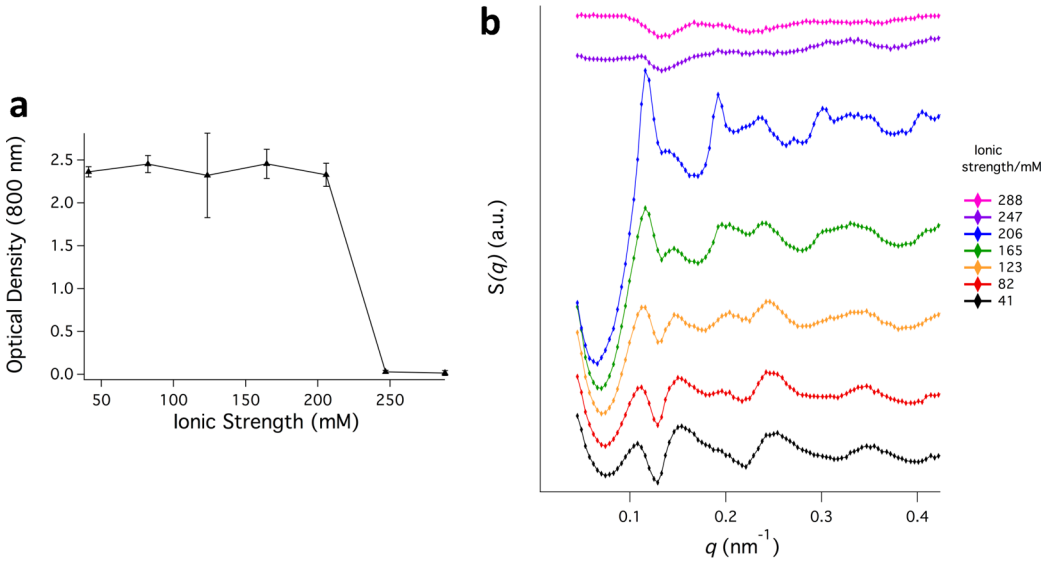

Figure 2. Higher order assembly of $P22_{E2}$ wiffleball (WB) with G6 dendrimer at various ionic strengths. (a) Light scattering (monitored at 800 nm) and (b) extracted structure factors from small-angle X-ray scattering measurements of $P22_{E2}$ WB capsids assembled with 1000× G6 dendrimer at various ionic strengths. The emergence of sharp peaks at I = 206 mM is indicative of long-range ordering. Structure factor diminishes at ionic strengths above 206 mM, indicating reduced interparticle interactions.

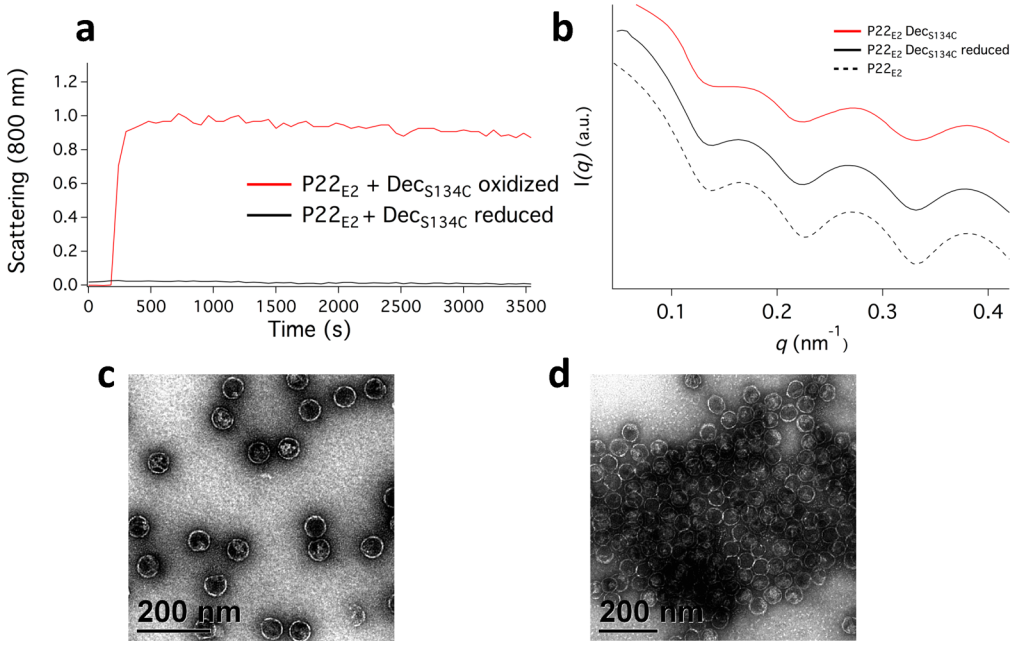

Figure 3. Assembly of $P22_{E2}$ wiffleball (WB) with Dec_{S134C}. (a) Light scattering (monitored at 800 nm) of $P22_{E2}$ WB capsids mixed with Dec_{S134C} either oxidized (red) or reduced (black). Only oxidized Dec_{S134C} causes assembly of $P22_{E2}$. (b) Small-angle X-ray scattering intensity of $P22_{E2}$ capsids (black dashed), mixed with Dec_{S134C}, either reduced (black solid) or oxidized (red), showing minimal change in intensity. The small shoulder at q = 0.10−0.12 nm^{-1} indicates the presence of short-range order. Transmission electron micrographs of (c) $P22_{E2}$ and (d) $P22_{E2}$ with oxidized Dec_{S134C}.

these biomolecule-based materials. The densely packed condensed phases could achieve exceptionally high protein concentrations, making it possible to run reactions at higher catalyst concentrations, thus increasing overall efficacy of the functional material.

RESULTS AND DISCUSSION

Ordered P22/Dendrimer Assemblies. Assemblies of the wiffleball morphology of $P22_{E2}$ capsids ($P22_{E2}$; Supplemental Figure S1) displaying long-range order were templated using generation 6 amine-terminated poly(amidoamine) dendrimers. Under a range of ionic strength conditions, light scattering (LS) and small-angle X-ray scattering (SAXS) were used to detect interparticle interactions (*i.e.*, assembly) and long-range order, respectively. A wide ionic strength range (41−288 mM) was investigated in order to detect all phases of the mixture. This range was chosen to compare assembly behavior to the PC morphology previously studied.[38] LS experiments (turbidity) show that, upon mixing of $P22_{E2}$ and G6 at a 1:1000 ratio, interparticle assembly occurs under conditions where the ionic

DOI: 10.1021/acsnano.8b00528
ACS Nano 2018, 12, 3541−3550

strength (I) is 206 mM or below (Figure 2a). In all assembled samples, the $P22_{E2}$ is located in the assembled sample, with no free $P22_{E2}$ detectable in the supernatant (Supplemental Figure S2). When $P22_{E2}$ and G6 are mixed at ionic strengths above 206 mM, no increase in turbidity was detected by LS, indicating no significant interparticle interactions. The length over which these interactions exist is explained by the Debye screening length, κ^{-1}:

$$\kappa^{-1} = \sqrt{\frac{\varepsilon_0 \varepsilon_r k_B T}{2 N_A e^2 I}}$$

where ε_0 is the vacuum permittivity, ε_r is the relative permittivity of the solution, k_B is the Boltzmann constant, T is the absolute temperature, N_A is Avogadro's number, e is the elemental charge, and I is the ionic strength. Turbidity is seen down to a Debye length of 0.67 nm, which corresponds to I = 206 mM. If I is increased further, thus decreasing the Debye length, interactions are screened.

Samples were interrogated using SAXS, which measures scattering due to the particle shape in solution (form factor), as well as the interactions between particles (structure factor). The scattering from the $P22_{E2}$ capsid alone in solution shows a form factor characteristic of a sphere (Figure 3b, black dashed trace). The structure factor data for the G6-mediated assembly of $P22_{E2}$ were extracted from the experimental data after deconvolution of the $P22_{E2}$ form factor (Supplemental Figure S3 and previous work).[38] When the $P22_{E2}$/G6 assembly was made in ionic strengths in the range 41−206 mM, a peak appeared at q = 0.078−0.108 nm^{-1}, indicating the presence of interparticle interactions. The assemblies that form at ionic strengths in the range I = 41−165 mM are structurally amorphous, as indicated by the peak broadness and the absence of higher order peaks. However, with increasing ionic strength (Figure 2b, bottom to top) the primary diffraction peak at q = 0.078−0.108 nm^{-1} narrows and sharpens considerably. The profile at I = 206 mM (q = 0.1163 nm^{-1}, blue trace) signifies the formation of a structure exhibiting long-range order and possessing a face-centered cubic structure (Supplemental Figure S4) with a domain size (*i.e.*, coherence length) of approximately ∼450 nm (Supplemental Table S1). Because dynamic light scattering (DLS) data show particles in the micrometer size range, it is likely that larger assemblies exist that contain multiple crystalline domains (Supplemental Figure S5). The SAXS measurements also confirm that mixtures of $P22_{E2}$ and G6 at I values above 206 mM do not interact to form higher order structures (Figure 2b, violet and magenta traces), as indicated by diminished diffraction peaks in the structure factor. These data suggest that there is a conditional window where the formation of materials with long-range order is optimal as is commonly observed in assemblies of oppositely charged particles.[25,38,46] Assembling particles into arrays that exhibit long-range order is achieved by avoiding kinetic traps,[46] which occur under low ionic strength conditions where charge attractions between the VLP and G6 dendrimer are strong. Increasing the ionic strength lowers the magnitude of these potential minima to a value closer to the kinetic energy of the particles such that VLPs and G6 can rearrange into more ordered structures.[38] Of the ionic strength solutions that produce assemblies chosen for this study (at I = 41−206 mM), 206 mM displayed the sharpest diffraction peaks consistent with a face-centered cubic (FCC) structure. Assembly at ionic strengths below 206 mM produced more amorphous assemblies due to the formation of kinetically trapped structures, while ionic strengths above 206 mM did not form assemblies because charges are shielded, thus preventing interparticle electrostatic interactions. When materials assembled in I = 206 mM or below were pelleted *via* centrifugation and resuspended in high ionic strength buffer (I = 329.2 mM), the turbidity (LS) and structure factor (SAXS) disappeared (Figure 4a, red trace), a clear indication of

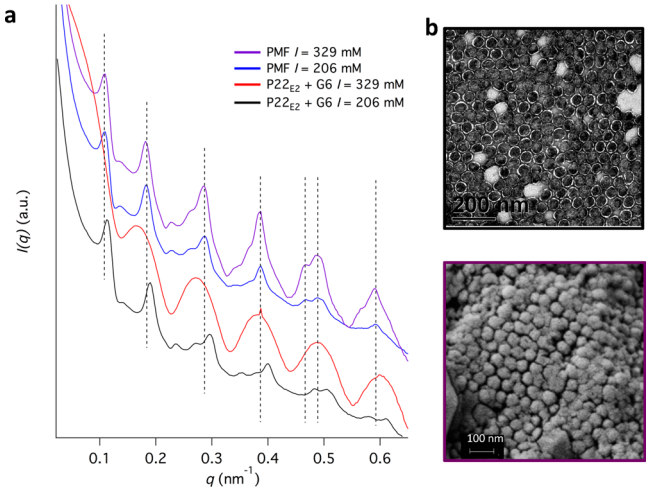

Figure 4. Small-angle X-ray scattering of the templated assembly of a protein macromolecular frameworks. (a) $P22_{E2}$ assembled with G6 (black) results in an array exhibiting long-range order, as is evident by the formation of diffraction peaks (q = 0.0115 Å; 0.0019 Å). When this ordered assembly is transferred into a high ionic strength buffer (red), structure factor contributions are significantly reduced, indicating disassembly. Dec_{S134C} (blue) addition to a G6-templated assembly of $P22_{E2}$ locks the array into place and shows preservation of long-range order and a shift in peak positions (vertical dashed lines). This shift corresponds to an increase in the nearest neighbor distance from 65.5 nm to 68.4 nm. When PMFs are transferred into high ionic strength buffer (violet) assembly, long-range order and peak position are preserved. (b) TEM image of P22/dendrimer assembly corresponding to the black trace. (c) SEM image of PMFs corresponding to the violet trace.

disassembly due to charge shielding. Although long-range order can be achieved, the resulting structures cannot be maintained in ionic strengths above the threshold ionic strength.

Creating Amorphous P22 Assemblies *via* Capsid Linker Protein. Using an entirely different approach toward guiding interparticle interactions to effect assembly, we used our previously developed ditopic protein linker (Dec_{S134C}) that binds the P22 capsid at multiple symmetry-specific sites[40] with high affinity.[42,43] This approach is conceptually similar to the designed lattice structures achieved by the geometrical arrangement of metal ligand interactions in MOF materials. Here the capsids are the equivalent of the metal ion or metal cluster and Dec_{S134C} is the equivalent of the organic chelate linker. In the case of MOFs, the choice of organic linker and metal dictates the geometry of the lattice. Our ditopic linker protein, which forms intermolecular disulfide bonds at its C-terminus, binds *via* its N-terminus tightly to 60 symmetry-related quasi 3-fold sites of the P22 icosahedral capsid *via* strong interactions in the expanded and wiffleball morphologies[40,43] (Supplementary Figure S6). We have previously shown that ditopic Dec_{S134C} strongly linked wild-type EX capsids

DOI: 10.1021/acsnano.8b00528
ACS Nano 2018, 12, 3541−3550

together into a higher order assembly, but which did not result in any measurable long-range order.[43]

Dec_{S134C} interaction with $P22_{E2}$ produced a similar amorphous assembly. An increase in turbidity was observed when an excess of Dec_{S134C} was mixed with $P22_{E2}$ capsids. However, under reducing conditions with non-disulfide-linked Dec ($Dec_{S134C\text{-}red}$) no interparticle-mediated interaction was detected by light scattering (Figure 3a). SAXS analysis of Dec_{S134C}-mediated assemblies showed that ordered arrays are not produced, as is evident from the absence of structure factor contributions in the SAXS intensity plot (Figure 3b). Additional treatment with heat or reducing agent did not result in an annealed and ordered structure. This lack of order can be understood given the tight binding of Dec to the P22 capsid (K_D = 9.2 ± 0.5 nM), a consequence of a fast on-rate and a slow off-rate.[42] Because of this fast on-rate, mixing of $P22_{E2}$ with Dec_{S134C} results in the rapid formation of a highly interconnected material and, because of the slow off-rate, results in a kinetically trapped disordered material. Thus, while the Dec_{S134C} linker directs the assembly of $P22_{E2}$ and produces a highly stable network of interconnected proteins, the resultant protein assembly lacks long-range order, consequently making it difficult to structurally characterize.

Protein Macromolecular Frameworks. Protein macromolecular frameworks of $P22_{E2}$ exhibiting long-range order were created by combining the two construction methods described above. First, ordered assemblies of $P22_{E2}$ particles were created using G6 dendrimers; then this templated structure was cemented into place with the addition of Dec_{S134C}. $P22_{E2}$ capsids were mixed with an excess of G6 dendrimers at a ratio of 1:1000 under ideal ionic strength conditions (I = 206 mM), as described above (Figure 4a, black trace). The assemblies were then exposed to an excess of Dec_{S134C} (Figure 4a, blue trace). The solution remained turbid, suggesting that the assemblies did not dissociate upon Dec_{S134C} addition. SAXS data revealed that the long-range order of the structure was preserved, as is evident by the retention of peaks associated with the structure and a similar domain size (Supplemental Table S1). After cementing the G6-mediated assemblies with Dec_{S134C}, the material was centrifuged and resuspended in high ionic strength buffer (I = 329 mM) to remove the G6 template and yield the final PMF (Figure 4a, purple trace). The structure and domain size were also conserved in the PMF under these conditions, whereas G6-mediated assemblies (no Dec_{S134C}) were disassembled (Figure 4a, red trace) under these conditions. Interestingly, a shift toward lower q was observed in the SAXS peaks after Dec_{S134C} addition (q = 0.1153 nm^{-1} shifted to q = 0.1105 nm^{-1} [vertical dashed line]), indicating an increase in the interparticle spacing once cementing of the lattice occurred. This corresponds to a change in the lattice parameter from a = 92.6 nm to a = 96.8 nm and a nearest neighbor (NN) distance change from NN = 65.5 nm to NN = 68.4 nm. The q values remained the same after increasing the ionic strength to remove the G6 dendrimer; thus, assembly and long-range order were maintained in ionic strength conditions in which G6-mediated assemblies were not. A two-dimensional hexagonal arrangement of particles was observed by negative stain transmission electron microscopy (TEM) of G6-mediated assemblies (Figure 4b) and scanning electron microscopy (SEM) of PMFs (Figure 4c), but were not observed in samples of only Dec_{S134C}-mediated assembly (Figure 3d). These microscopy images alone do not confirm ordered close packing, due to the possibility of drying effects as well as the difficulty in assessing multiple particle layers, but instead support the SAXS data that indicate the formation of a close-packed assembly of particles. Because of this potential for drying effects, structure sizes were determined by DLS, showing PMF assemblies in the micrometer range (Supplementary Figure S5).

The increase in the PMF lattice parameter after Dec_{S134C} addition indicates that the ditopic Dec_{S134C} linkers can access the interparticle volume within the bulk assembly, bind and cross-link $P22_{E2}$ capsids, while maintaining the FCC structure. While an atomic resolution structure of Dec is not available, we estimate, from reported cryoTEM data, that Dec is at least 4 nm from the N- to the C-terminus. Therefore, one ditopic Dec_{S134C} linker, which is a head-to-head dimer of Dec_{S134C}, could be extended as much as 8 nm from the P22 surface[40] and therefore is likely compressed in the structure, where it links nearest neighbor capsids. Analysis of SDS PAGE gels by densitometry revealed a ratio of incorporated Dec_{S134C} to $P22_{E2}$ of 47 ± 3 Dec_{S134C} trimers per $P22_{E2}$ capsid, which is in close agreement with the known 60 tight binding sites available per capsid (Supplemental Figure S7). These data suggest that Dec_{S134C} can access the interior of the G6-mediated assemblies, not just the surface, and act as capsid cross-linkers, yielding robust PMFs.

To verify G6 removal from PMFs during high ionic strength resuspension, amino acid analysis was performed, by which we can determine the amount of both $P22_{E2}$ and G6. Samples were acid hydrolyzed, and then derivitized primary and secondary amines were quantified by HPLC using amino acid and G6 standard curves (Supplemental Figure S8; Supplemental Tables S2 and S3). G6-mediated assemblies and PMFs assembled under ideal ionic strength conditions (I = 206 mM) contained 54.8 ± 2.25 and 55.6 ± 2.29 G6 molecules per $P22_{E2}$ capsid, respectively, indicating that G6 remains within the lattice after Dec_{S134C} binding. However, PMFs that were resuspended and washed in high ionic strength buffer showed only residual amounts of G6 (5.7 ± 0.23) (Supplementary Table S2). In contrast to G6-mediated assemblies using the PC morphology previously reported, which showed a ratio of 20:1 G6:$P22_{E2}$ PC,[38] the WB morphology of $P22_{E2}$ in this study exhibits a higher dendrimer to capsid ratio. This higher ratio could be due to the ability of G6 to access the capsid interior through the 10 nm pores and interact with the highly negatively charged interior surfaces.[47] The fact that G6-mediated assemblies and PMFs before high ionic strength resuspension show the same G6 ratio indicates that G6 remains bound at I = 206 when Dec_{S134C} is added to assemblies, suggesting that the G6 molecules either do not occupy the Dec binding site of $P22_{E2}$ capsids or can shift to accommodate Dec binding, but remain present in the PMFs, probably to ensure charge balance in the assembly. Importantly, when PMFs are resuspended in high ionic strength buffer, G6 is removed from the material. This result is partially expected, as high ionic strength conditions (*i.e.*, I = 349 mM) disrupt the electrostatic interactions between capsid and dendrimer (but not between Dec and the capsid), and also suggests that the pores within the framework between $P22_{E2}$ particles are large enough to allow removal of the 6.7 nm G6 dendrimer. PMFs that were treated with reducing agent resulted in a significant reduction in scattering, consistent with the expected disassembly of the structure being connected through disulfide bonding (Supplemental Figure S9). Together, these data show that an ordered lattice of protein material, comprising virus-like particles, can be electrostatically tem-

DOI: 10.1021/acsnano.8b00528
ACS Nano 2018, 12, 3541−3550

plated using cationic dendrimers and then cemented into an ordered protein macromolecular framework with noncovalent protein cross-linkers followed by removal of the dendrimer template.

Catalytically Active PMFs. A distinctive feature of PMFs is the ability to impart functionality to $P22_{E2}$ building blocks before PMF construction. Here, PMFs were functionalized by genetically preprogramming $P22_{E2}$ capsids to encapsulate enzymes, which resulted in a catalytically active molecular framework composed solely of protein material. Catalytic PMFs were constructed using $P22_{E2}$ capsids encapsulating multiple copies of the enzyme CelB, a glycosidase from the hyperthermophilic Archaeon *Pyrococcus furiosus* (Supplemental Figure S10).[48] One advantage of encapsulating enzymes inside of P22 building blocks within the PMF is the ease with which they are concentrated into a highly condensed-phase material and their capacity to be separated from reaction components. P22 particles free in solution can also be condensed to high concentrations through centrifugation at ultrahigh speeds. However, once mixed with substrate, a second ultracentrifugation step, or other separation technique, must be performed to separate catalysts from reaction components. In addition to the ease with which PMFs are separated from reaction components, assembling catalytic P22 VLPs into PMFs does not affect enzymatic activity, suggesting small-molecule diffusion through the framework is not hindered (Supplemental Figure S11). The close packing of $P22_{E2}$ particles in the PMF results in a CelB concentration of ~1 mM (70 mg/mL) within the framework material and local concentrations of CelB within each P22 of 2 mM (140 mg/mL). This local concentration of enzymes is well beyond that which most enzymes can functionally be used and highlights the advantage of combining capsid encapsulation with PMF assembly to create highly active functional materials. Due to the modular nature of this system, where packaging of the catalytic material on the VLP interior does not compromise the ability to form higher order structures, the interior and exterior modifications are independent and suggest a wide applicability.[38] To demonstrate the ease and functional benefit of material condensation, PMF_{E2}-CelB samples, either as-assembled or condensed PMF phases, were assayed for their ability to catalyze the ester hydrolysis of 4-nitrophenyl α-D-glucopyranoside (PNPG) by monitoring the absorbance of the 4-nitrophenol product at 405 nm. For condensed-phase experiments, activity assays were conducted at 60 °C, as hyperthermophilic CelB significantly increases its catalytic activity at elevated temperatures. Upon addition of the same volume of catalyst (different concentrations) to equivalent amounts of substrate, concentrated PMFs (10×) showed an increase in product formation of 1.978 ± 0.019 μmol/s as compared to 0.232 ± 0.001 μmol/s for the nonconcentrated PMF_{E2}-CelB (Figure 5). This is reflective of the ability to maintain high concentrations of active catalysts in the PMFs upon condensation, unlike homogeneous systems, where a significant volume is required to maintain and disperse stable enzyme catalysts. Here, we maintain the same catalytic ability of the enzymes and demonstrate the ease with which the material is condensed, either through brief, gentle centrifugation or by merely allowing the material to settle. At the assay temperature of 60 °C the PMFs remained assembled, as determined by dynamic light scattering measurements, which is significant because many proteins have T_M values below 60 °C (Supplemental Figure S12). In activity retention studies PMF_{E2}-CelB showed 87.7% and 75.0% activity preservation after freezing and lyophilization, respectively, without the material breaking down into constituent building blocks (Supplemental Figure S13). While these findings do not indicate if the FCC lattice is maintained, it does signify the robustness of PMFs as a functional material. Additionally, normalized activity (per enzyme) was unchanged after three consecutive catalytic rounds, while retaining 73.8% and 72.0% of protein material after one and two catalytic rounds, respectively (Supplemental Figure S14).

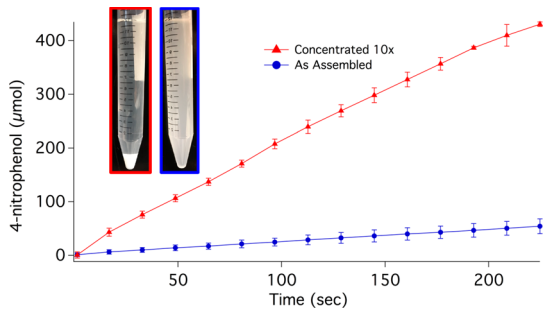

Figure 5. Catalytic activity of $P22_{E2}$-CelB glycosidase PMFs. $P22_{E2}$-CelB particles assembled in PMFs were assayed for their ability to cleave 4-nitrophenyl-β-D-glucopyranoside and produce 4-nitrophenol. Catalytic PMFs were assayed either as-assembled (blue) or condensed 10-fold (red).

CONCLUSION

We have shown the creation of a functional protein macromolecular framework through dendrimer-templated assembly of virus-like particles into structures displaying long-range order followed by the addition of an engineered ditopic capsid decoration protein, which acts as an inter-VLP linker to lock the structures in place. Because Dec_{S134C} binds in a symmetry-specific manner, we equate these molecules to the organic chelates in a MOF. However, in our case, addition of the linker alone does not produce an ordered lattice due to the formation of kinetic traps but can be achieved by first creating a dendrimer template. Because Dec_{S134C}-mediated assemblies do not anneal to form ordered structures, the order in which linker molecules are added is critical. Removal of the template yields robust PMFs that are stable in conditions under which nonlocked structures disassembled. The resultant material is a three-dimensionally ordered lattice composed solely of protein building blocks.

An impressive feature of PMFs is the ability to undergo lattice expansion upon Dec_{S134C} locking, while maintaining the FCC structure. This structure retention highlights the stability of the lattice, as well as the possibility of engineering Dec to modulate the lattice further, thus controlling the porosity of the material. Another benefit of PMFs is the ease with which they are created. Unlike traditional protein crystals, which can take time to grow and optimize, PMFs assemble immediately upon mixing $P22_{E2}$ with linker molecules. Additionally, since the exterior of the VLP does not need to be changed to functionalize the interior, this assembly design can potentially be applied to any $P22_{E2}$ VLP, regardless of what is encapsulated on the interior. Because P22 VLP building blocks can be genetically preprogrammed or chemically modified to encapsulate a wide range of cargo molecules, the resultant PMFs are modular in nature. This modularity allows the catalytic function

DOI: 10.1021/acsnano.8b00528
ACS Nano 2018, 12, 3541−3550

to be tailored without sacrificing structure, which is challenging in many other structurally defined materials.

A hallmark of bulk catalytic materials including PMFs is their condensed-phase nature, which not only allows for the highly efficient use of the reaction volume but also allows the material to be easily separated from solution and thus recovered from substrates and products, and subsequently reused without loss of activity. We have further demonstrated functional robustness of the material by showing that catalytic PMFs retain activity after heating, cooling, and lyophilization. This work has demonstrated the construction of a class of bioinspired materials in which biological building blocks can be genetically preprogrammed to achieve desired structural and functional materials properties.

METHODS

Particle Preparation. *$P22_{E2}$.* *E. coli* strains with incorporated pRSF duet expression vector containing the P22 coat protein with the Ecoil-2x peptide fused to the C-terminus[38] and the truncated version (residues 142−303) of P22 scaffolding protein in multiple cloning sites 1 and 2, respectively, were grown in LB medium at 37 °C in the presence of kanamycin (30 μg/mL) to maintain selection for the plasmid. Protein expression was induced by addition of isopropyl β-D-thiogalactopyranoside (IPTG) to a final concentration of 0.3 mM once the cells reached mid log phase (OD_{600} = 0.6). Cultures were grown an additional 4 h after induction with IPTG, and then the cells were harvested by centrifugation at 4500*g*, resuspended in minimal phosphate-buffered saline (PBS), and stored at −80 °C.

The *E. coli* cell solution was thawed at room temperature, then diluted in lysis buffer (50 mM sodium phosphate, 100 mM sodium chloride, pH 7) at a ratio of 5−10 mL lysis buffer per g of cell pellet. After rocking with DNase, RNase, and lysozyme for 30 min at room temperature, cells were lysed *via* sonication. The solution was centrifuged at 12000*g* for 45 min to remove cellular debris, then centrifuged at 45000 rpm (F50L-8×39 rotor) through a 35% sucrose cushion. Pelleted particles were resuspended in minimal lysis buffer, then applied to a Sephacryl-500 size exclusion chromatography column connected to a Biorad FPLC. Fractions containing P22 VLPs were pooled and concentrated *via* ultracentrifugation.

$P22_{E2}$-CelB. *E. coli* strains with incorporated (1) pRSF duet expression vector containing the gene encoding P22 CP with the Ecoil-2x peptide fused to the C-terminus[38] in multiple cloning site (MCS) 1 (MCS 2 empty) and (2) pBad expression vector containing the gene encoding the truncated SP fused to the C-terminus of CelB[48] (NcoI/SacI) were grown in LB medium at 37 °C in the presence of kanamycin (30 μg/mL) and ampicillin (50 μg/mL) to maintain selection for the plasmids. CelB-SP expression was induced by addition of L-arabinose to a final concentration of 13.3 mM once the cells reached mid log phase (OD_{600} = 0.6). After 4 h CP expression was induced by addition of IPTG to a final concentration of 0.3 mM. Cultures were grown an additional 2 h after induction with IPTG, and then the cells were harvested by centrifugation at 4500*g*, resuspended in minimal PBS, and stored at −80 °C. P22 particles were purified as stated above.

Dec_{S134C}. *E. coli* cultures with incorporated pET duet plasmid containing Dec were induced as described above and grown overnight. After centrifugation of cells at 4500g, the supernatant was retained, filtered, and applied to a 5 mL Roche cOmplete His-Tag purification column. Nonspecific binders were removed with 20 mM imidazole. Histadine-tagged protein was eluted with a 20−500 mM imidazole gradient. Fractions containing Dec_{S134C} were pooled and dialyzed against assembly buffer.

Generation 6 Poly(amidoamine) Dendrimers. PAMAM dendrimer (ethylenediamine core) generation 6.0 in 5% methanol solution was purchased from Sigma-Aldrich. Stock solutions of G6 dendrimer and appropriate buffer were prepared at a 1:4 ratio.

Particle Characterization. *SDS PAGE.* Protein samples were mixed with 4× SDS loading buffer containing dithiothreitol (DTT) and denatured in a 100 °C water bath for 5 min. Samples were loaded onto a 12% acrylamide resolving gel (5% acrylamide stacking gel) and separated using a constant current of 35 mA for approximately 1 h. Gels were stained with Coomassie blue stain, then destained. Images were taken on a UVP MultDoc-IT digital imaging system.

P22 Expansion to Wiffleball Morphology. $P22_{E2}$ capsids were expanded to the wiffleball morphology by heating in a 75 °C water bath for 25 min, then cooled at 4 °C. Samples were centrifuged at 17000*g* for 5 min to remove aggregated protein, then centrifuged at 45000 rpm to concentrate capsids and to remove SP. A 10 μL portion of each of heated and nonheated ∼1 mg/mL $P22_{E2}$ sample were mixed separately with 5 μL of nondenaturing protein loading dye and loaded into a 0.8% agarose gel. A constant voltage of 65 V was applied for 3 h. Gels were stained and imaged as described above.

Size Exclusion Chromatography Coupled with Multiangle Light Scattering. Samples were separated using a WTC-200S5 (Wyatt Technologies) size exclusion column utilizing an Agilent 1200 HPLC at a 0.7 mL/min flow rate in 50 mM phosphate, 100 mM sodium chloride, and 200 ppm of sodium azide pH 7.2 buffer. For each sample, three 25 μL injections were loaded onto the column with a total run time of 30 min. Samples were detected using a Wyatt HELEOS multiangle laser light scattering detector and an Optilab rEX differential refractometer (Wyatt Technology Corporation). The average molecular weight, M_w, was calculated with Astra 5.3.14 software (Wyatt Technology Corporation) based on the molecular weight distribution.

Transmission Electron Microscopy. Individual Particles. A 5 μL amount of each sample (diluted in water to 0.1−0.3 mg/mL) was applied to a glow discharged Formvar-coated grid (Electron Microscopy Sciences). After 30 s excess liquid was wicked away with filter paper, then immediately stained with 5 μL of 2% uranyl acetate. Excess stain was wicked away with filter paper after 25 s, then allowed to air-dry. Images were taken on a JEOL 1010 transmission electron microscope at an accelerating voltage of 100 kV.

Assembled Particles. Assemblies were centrifuged at 17000*g* briefly, then resuspended in ultrapure water and vortexed for 5 s at high-speed 2×. Grids were then prepared as described above.

SEM. Assemblies were centrifuged on a benchtop centrifuge, then resuspended in water (2×). A 30 μL amount of sample was deposited on a silicon wafer, dried with nitrogen, then quickly washed with water 2×. Silicon wafers were secured on an aluminum stud using double-sided carbon tape, then coated with 3 nm of gold/palladium using a Denton sputter coater. Assemblies were imaged using a Zeiss Auriga 60 focused ion beam scanning electron microscope and detected on a through-the-lens detector.

Assembly. *Light Scattering.* $P22_{E2}$ samples were buffer exchanged into the following ionic strength buffers using Bio-Rad Micro Bio-Spin P-30 columns: 10 mM sodium phosphate, 20 mM sodium chloride (I = 41 mM), 20 mM sodium phosphate 40 mM, sodium chloride (I = 82 mM), 30 mM sodium phosphate, 60 mM sodium chloride (I = 123 mM), 40 mM sodium phosphate, 80 mM sodium chloride (I = 165 mM), 50 mM sodium phosphate, 100 mM sodium chloride (I = 206 mM; assembly buffer), 60 mM sodium phosphate, 120 mM sodium chloride (I = 247 mM), 70 mM sodium phosphate, 140 mM sodium chloride (I = 288 mM), 80 mM sodium phosphate, 160 mM sodium chloride (I = 329 mM). All buffers were adjusted to pH 7.0. Turbidity measurements to monitor the assembly of particles were performed on an Agilent 8453 UV−vis spectrophotometer fitted with an eight-position multicell transport. After blanking with the appropriate buffer, solutions of P22 (at 1.0−2.0 mg/mL) were monitored at 800 nm for 3−4 min; then linker solution was added and mixed thoroughly. Assemblies were monitored for 30−60 min. For P22 assemblies with G6 dendrimer: G6 (diluted in appropriate ionic strength buffer from methanol stock solution) was added at a 1000 times excess of dendrimer per P22 (final amount methanol = 5%) or a methanol buffer control. To measure the amount of material remaining in the supernatant and not associated with assemblies, mixtures of $P22_{E2}$ (buffer exchanged in appropriate buffer) and G6 dendrimer (diluted in appropriate buffer) at various ionic strengths were centrifuged in 2 mL Eppendorf tubes at 21000*g* for 3 min to pellet assembled material. A

DOI: 10.1021/acsnano.8b00528
ACS Nano 2018, 12, 3541−3550

70 μL portion of the total 170 μL sample was removed from the top of the solution *via* pipetting to avoid pellet resuspension. G6 dendrimer control samples were measured by diluting G6 dendrimer with the appropriate buffer to the same dilution as in assembled samples. The $P22_{E2}$ (I = 206 mM) control was measured by diluting with assembly buffer to the same dilution as in assembled samples. Supernatants, G6 controls, and the $P22_{E2}$ control were analyzed by measuring the net absorbance at 280 nm (baseline corrected *via* subtraction of absorbance from 800−850 nm). PMFs were created by adding Dec_{S134C} to P22 to a final ratio of 2:1 Dec trimer:P22-Dec binding site (*i.e.*, 160:1 molar ratio). Samples were washed of free linker molecules *via* centrifugation at low *g*, removal of supernatant, then resuspension in appropriate buffer solution.

SAXS. Small-angle X-ray scattering data were collected at the Advanced Photon Source at Argonne National Laboratory at beamlines 12-ID-B and 12-ID-C/D at 14 keV. Samples were continuously moved using a syringe pump system to minimize beam damage and subjected to a 1 s exposure time, 2 s interval, and 20 total shots per sample and detected by a Pilatus 2M detector. The scattering angle was calibrated using silver behenate as a standard. 2D images were then converted to 1D curves, and the 20 curves for each sample were then averaged. The background due to the sample buffer was measured separately and subtracted from the averaged data to give intensity $I(q)$. Structure factors $S(q)$ were extracted from $I(q)$ data as described previously.[38] Briefly, $I(q)$ is given as

$$I(q) = k(P(q) + c/q^n)S(q)$$

where k is a scaling constant, q (=$4\pi \sin(\theta)/\lambda$) is the scattering vector, λ is the wavelength of incident X-ray (0.8856 Å), and θ is half of the scattering angle. $P(q)$ is the form factor of a capsid and $S(q)$ is the structure factor, which arises from the assembly structure of capsids. The term c/q^n is a power-law function used to model the diffuse scattering, which arises from lattice imperfections, where c and n are constants. Because variation of particle arrangements as a function of ionic strength is the focus of Figure 2, we report $S(q)$ instead of $I(q)$, which was obtained by dividing $I(q)$ by $P(q) + c/q^n$. If the diffuse scattering was not taken into consideration, $S(q)$ would not have been obtained correctly.

The crystalline domain size was calculated from the full width at half-maximum (fwhm) of the first-order diffraction peak using the Scherrer equation[49−51]

$$d = \frac{K\lambda}{\beta \cos\theta}$$

where K is the Scherrer constant (we use 0.9 for a roughly equitant crystallite) and β is the fwhm of a diffraction peak in radians. Instrumental resolution Δq_{inst}, which leads to peak broadening, was taken into account with the assumption that the observed peak is a Gaussian function convoluted with a Gaussian instrumental resolution function. Then, the resolution-corrected fwhm of a sample peak, Δq_{samp}, is given by the following form:

$$\Delta q_{samp} = \sqrt{\Delta q_{obs}^{\ 2} - \Delta q_{inst}^{\ 2}}$$

where Δq_{obs} is the fwhm of an observed diffraction peak and Δq_{inst} for our measurement is approximately 0.0005 $Å^{-1}$.

Densitometry. A 10 μL amount from three separately assembled PMF (dendrimer removed) samples was each mixed with 4 μL of SDS loading dye and separated on a 12% SDS PAGE gel as described above. The relative intensities of the coat protein and Dec_{S134C} bands were analyzed using ImageJ software. A single band was quantified for the CP, while two bands were quantified for Dec_{S134C}, as both have been observed in samples of Dec_{S134C} alone. Standard curve values of P22:Dec_{S134C} ratios were experimentally determined by mixing P22:Dec_{S134C} at 1:30, 1:40, 1:60, 1:80, and 1:160. The number of Dec_{S134C} trimers incorporated into PMFs per P22 was determined by using the linear fit line.

Quantification of G6 Dendrimer/P22 Ratio in G6-Mediated Assemblies and PMFs. The amount of G6 dendrimer incorporated in assembled samples was determined by quantifying the amount of both dendrimer and P22 by an amino acid analysis. Assembled samples were prepared (either dendrimer-only samples or PMF samples) as described above. G6-assembled samples were centrifuged at 5000*g* for 3 min and resuspended in assembly buffer (50 mM sodium phosphate, 100 mM sodium chloride, pH 7.0) to remove excess dendrimer. These assemblies were centrifuged a second time and then resuspended either in assembly buffer or in high ionic strength buffer (80 mM sodium phosphate, 160 mM sodium chloride, pH 7.0). PMFs were washed twice as described above with either assembly or high ionic strength buffer.

All samples were separately acid hydrolyzed at 145 °C for 2 h, followed by derivatization of amino acids with a fluorescent tag (6-aminoquinolyl-*N*-hydroxysuccinimidyl carbamate using the AccQ-Fluor reagent kit from Waters), and then 10 μL was injected onto reverse-phase HPLC to quantify each component. The elution peak attributed to hydrolyzed dendrimer, not seen in amino acid controls or P22 samples, was observed directly after the phenylalanine peak. The concentrations of G6 in experimental samples were determined using the G6 dendrimer standard curve (G6 dendrimer peak areas obtained from 500, 1500, and 5000 nM). $P22_{E2}$ concentrations were also quantified through amino acid analysis. Briefly, the picomoles of each amino acid for each sample was determined from a standard curve and was converted to a fraction pmol. The number of each amino acid was experimentally determined by multiplying the fraction pmol by the expected number of total residues and compared with the theoretical number of each amino acid. For example, $P22_{E2}$ coat protein has 438 expected amino acids, excluding cysteines and tryptophans. In PMFs, the expected number of amino acids is 495, excluding cysteines and tryptophans, which are not reliably detectable by amino acid analysis, as determined by calculating the ratio of 47 Dec_{S134C} trimers per $P22_{E2}$ WB (CP:Dec_{S134C} = 360/141 per $P22_{E2}$ WB). Total % error for each sample was calculated by averaging the nonabsolute value of all % errors for each amino acid:

$$\left(\frac{(\text{experimental} - \text{theoretical}}{\text{theoretical}}\right) \times 100$$

PMF Reduction Assay. The ability to disassemble PMFs (no G6 dendrimer) in the presence of reducing agent was determined by measuring light scattering, which decreases upon disassembly. Measurements were recorded for $P22_{E2}$ and PMF samples in the presence or absence of 100 mM DTT purchased from Promega. All samples (~1 mg/mL) were heated for 2.5 h at 45 °C. Spectra were collected for samples before and after DTT heat treatment. Because PMFs eventually settle out of solution, all samples were mixed *via* pipetting immediately before data collection.

CelB Glycosidase Enzyme Assay. All CelB enzyme assays were monitored using an Agilent 8453 UV−vis spectrophotometer fitted with an eight-position multicell transport using PNPG as a substrate. Formation of the 4-nitrophenol (4-NP) product was monitored by recording the absorbance at 405 nm. Absorbances were converted to moles 4-NP using an experimentally derived extinction coefficient (pH 7.0) of 8.97 mM^{-1} cm^{-1}.

Condensed Catalyst Activity. Equal volumes and concentrations of PMF_{E2}-CelB samples were centrifuged at 5000*g* for 3 min. Supernatants were removed and resuspended in either the original volume or a 10-fold lower amount of buffer. A 4 μL amount of each sample was added to a quartz cuvette containing 1996 μL of 20 mM PNPG preheated to 60 °C. Absorbance at 405 nm was monitored every 15 s while the cuvette was kept at 60 °C. Assays were conducted in triplicate. Absorbances from cuvettes containing substrate but no enzyme were measured and subtracted from experimental assays. All assays were performed in triplicate.

Reusability. PMF_{E2}-CelB samples were assembled as described above. To expose PMF_{E2}-CelB to catalytic cycles, PNPG was added to samples such that the final concentration was 20 mM. After 1 h, samples were centrifuged 2× at 5000*g* for 3 min to separate PMF_{E2}-CelB from substrate and products, then resuspended in buffer. The presence of product was verified by measuring the absorbance at 405 nm (and also by the dark yellow color). PMF_{E2}-CelB samples were

DOI: 10.1021/acsnano.8b00528
ACS Nano 2018, 12, 3541−3550

used as a catalyst, then collected a total of three times. To monitor enzyme rate, 20 μL of PMF_{E2}-CelB material (taken from stock samples that had been reacted with substrate for 0, 1, or 2 cycles) was added to 480 μL of a 20.8 mM PNPG solution in 50 mM sodium phosphate, 100 mM sodium chloride, pH 7.0. At time points 15, 30, 45, and 60 min 10 μL was removed and diluted into either 90 μL (early in time course) or 490 μL (later in time course) of 50 mM sodium phosphate, 100 mM sodium chloride, pH 7.0, to significantly slow the reaction for accurate measurement, reduce the scattering contribution of PMFs, and dilute the 4-nitrophenol product to allow measurement in the appropriate intensity range. Absorbances were measured at 405 nm. Each assay was performed in triplicate. Catalytic rates were normalized to protein concentration by measuring the absorbance at 280 nm of the PMF_{E2}-CelB sample denatured in 6 M GuHCl.

Dynamic Light Scattering. The presence of free $P22_{E2}$-CelB particles, after assemblies were subject to heating, freezing, and lyophilization were measured by dynamic light scattering using a Zetasizer Nano Z (Malvern Instruments, Worcestershire, UK). Percent volumes were plotted as a function of size.

Percent Activity. Freezing. PMF samples were flash frozen in liquid nitrogen and then thawed at room temperature. Catalytic activity was monitored at room temperature as described above. Equal amounts of PMF sample, either frozen or nonfrozen, were added to the PNPG substrate and monitored by UV−vis.

Lyophilization. PMF samples were flash frozen in liquid nitrogen, then lyophilized on a Labconco Freezone 2.5 plus freeze-dryer overnight. Immediately before kinetics assays were performed, samples were resuspended in an equivalent amount of water to that present in the initial sample. Catalytic activity was monitored as described above and compared to activity of the same sample before lyophilization.

ASSOCIATED CONTENT

Supporting Information

The Supporting Information is available free of charge on the ACS Publications website at DOI: 10.1021/acsnano.8b00528.

Additional experimental data (PDF)

AUTHOR INFORMATION

Corresponding Author

*E-mail: trevdoug@indiana.edu. Tel: (812) 856-6936.

ORCID

Masaki Uchida: 0000-0003-0710-8834

Byeongdu Lee: 0000-0003-2514-8805

Trevor Douglas: 0000-0002-7882-2704

Notes

The authors declare no competing financial interest.

ACKNOWLEDGMENTS

K.M. was supported by a grant from the National Science Foundation (NSF-BMAT DMR-1507282). M.U. was supported by a grant from the U.S. Department of Energy, Office of Basic Energy Sciences, Division of Materials Sciences and Engineering (DE-SC0016155). T.D. would like to acknowledge support from the National Science Foundation under the Network for Computational Nanotechnology (NCN) program (award 1720625, Network for Computational Nanotechnology - Engineered nanoBIO Node). This research used resources of the Advanced Photon Source, a U.S. Department of Energy (DOE) Office of Science User Facility operated for the DOE Office of Science by Argonne National Laboratory under Contract No. DE-AC02-06CH11357. We thank the IU Electron Microscopy Center, the IU Nanoscale Characterization Facility, the IU Mass Spectrometry Facility, and the IU Laboratory for Biological Mass Spectrometry for access to their instrumentation.

REFERENCES

(1) Slater, A. G.; Cooper, A. I. Function-Led Design of New Porous Materials. *Science* **2015**, *348*.aaa807510.1126/science.aaa8075

(2) Busseron, E.; Ruff, Y.; Moulin, E.; Giuseppone, N. Supramolecular Self-Assemblies as Functional Nanomaterials. *Nanoscale* **2013**, *5*, 7098−7140.

(3) Liljestrom, V.; Mikkila, J.; Kostiainen, M. A. Self-Assembly and Modular Functionalization of Three-Dimensional Crystals from Oppositely Charged Proteins. *Nat. Commun.* **2014**, *5*, in press DOI: 10.1038/ncomms5445.

(4) Yaghi, O. M.; O'Keeffe, M.; Ockwig, N. W.; Chae, H. K.; Eddaoudi, M.; Kim, J. Reticular Synthesis and the Design of New Materials. *Nature* **2003**, *423*, 705−714.

(5) Ma, S.; Zhou, H.-C. Gas Storage in Porous Metal-Organic Frameworks for Clean Energy Applications. *Chem. Commun.* **2010**, *46*, 44−53.

(6) Lee, J.; Farha, O. K.; Roberts, J.; Scheidt, K. A.; Nguyen, S. T.; Hupp, J. T. Metal-Organic Framework Materials as Catalysts. *Chem. Soc. Rev.* **2009**, *38*, 1450−1459.

(7) Denny, M. S.; Moreton, J. C.; Benz, L.; Cohen, S. M. Metal−Organic Frameworks for Membrane-Based Separations. *Nature Reviews Materials* **2016**, *1*, 16078.

(8) Van de Voorde, B.; Bueken, B.; Denayer, J.; De Vos, D. Adsorptive Separation on Metal-Organic Frameworks in the Liquid Phase. *Chem. Soc. Rev.* **2014**, *43*, 5766−5788.

(9) Furukawa, H.; Cordova, K. E.; O'Keeffe, M.; Yaghi, O. M. The Chemistry and Applications of Metal-Organic Frameworks. *Science* **2013**, *341*.123044410.1126/science.1230444

(10) Sontz, P. A.; Bailey, J. B.; Aln, S.; Tezcan, F. A. A Metal Organic Framework with Spherical Protein Nodes: Rational Chemical Design of 3d Protein Crystals. *J. Am. Chem. Soc.* **2015**, *137*, 11598−11601.

(11) Song, W. J.; Tezcan, F. A. A Designed Supramolecular Protein Assembly with *in Vivo* Enzymatic Activity. *Science* **2014**, *346*, 1525−1528.

(12) Lian, X. Z.; Fang, Y.; Joseph, E.; Wang, Q.; Li, J. L.; Banerjee, S.; Lollar, C.; Wang, X.; Zhou, H. C. Enzyme-Mof (Metal-Organic Framework) Composites. *Chem. Soc. Rev.* **2017**, *46*, 3386−3401.

(13) Morris, W.; Briley, W. E.; Auyeung, E.; Cabezas, M. D.; Mirkin, C. A. Nucleic Acid-Metal Organic Framework (Mof) Nanoparticle Conjugates. *J. Am. Chem. Soc.* **2014**, *136*, 7261−7264.

(14) Kostiainen, M. A.; Pietsch, C.; Hoogenboom, R.; Nolte, R. J. M.; Cornelissen, J. Temperature-Switchable Assembly of Supramolecular Virus-Polymer Complexes. *Adv. Funct. Mater.* **2011**, *21*, 2012−2019.

(15) Nykypanchuk, D.; Maye, M. M.; van der Lelie, D.; Gang, O. DNA-Guided Crystallization of Colloidal Nanoparticles. *Nature* **2008**, *451*, 549−552.

(16) Park, S. Y.; Lytton-Jean, A. K. R.; Lee, B.; Weigand, S.; Schatz, G. C.; Mirkin, C. A. DNA-Programmable Nanoparticle Crystallization. *Nature* **2008**, *451*, 553−556.

(17) Straley, K. S.; Heilshorn, S. C. Independent Tuning of Multiple Biomaterial Properties Using Protein Engineering. *Soft Matter* **2009**, *5*, 114−124.

(18) Gonen, S.; DiMaio, F.; Gonen, T.; Baker, D. Design of Ordered Two-Dimensional Arrays Mediated by Noncovalent Protein-Protein Interfaces. *Science* **2015**, *348*, 1365−1368.

(19) Abe, S.; Ijiri, H.; Negishi, H.; Yamanaka, H.; Sasaki, K.; Hirata, K.; Mori, H.; Ueno, T. Design of Enzyme-Encapsulated Protein Containers by *in Vivo* Crystal Engineering. *Adv. Mater.* **2015**, *27*, 7951−7956.

(20) Sakai, F.; Yang, G.; Weiss, M. S.; Liu, Y. J.; Chen, G. S.; Jiang, M. Protein Crystalline Frameworks with Controllable Interpenetration Directed by Dual Supramolecular Interactions. *Nat. Commun.* **2014**, *5*, 463410.1038/ncomms5634.

(21) Asor, R.; Ben-nun-Shaul, O.; Oppenheim, A.; Raviv, U. Crystallization, Reentrant Melting, and Resolubilization of Virus Nanoparticles. *ACS Nano* **2017**, *11*, 9814−9824.

DOI: 10.1021/acsnano.8b00528
ACS Nano 2018, 12, 3541−3550

(22) Douglas, T.; Young, M. Host-Guest Encapsulation of Materials by Assembled Virus Protein Cages. *Nature* **1998**, *393*, 152−155.
(23) Falkner, J. C.; Turner, M. E.; Bosworth, J. K.; Trentler, T. J.; Johnson, J. E.; Lin, T. W.; Colvin, V. L. Virus Crystals as Nanocomposite Scaffolds. *J. Am. Chem. Soc.* **2005**, *127*, 5274−5275.
(24) Suci, P. A.; Klem, M. T.; Arce, F. T.; Douglas, T.; Young, M. Assembly of Multilayer Films Incorporating a Viral Protein Cage Architecture. *Langmuir* **2006**, *22*, 8891−8896.
(25) Kostiainen, M. A.; Hiekkataipale, P.; Laiho, A.; Lemieux, V.; Seitsonen, J.; Ruokolainen, J.; Ceci, P. Electrostatic Assembly of Binary Nanoparticle Superlattices Using Protein Cages. *Nat. Nanotechnol.* **2013**, *8*, 52.
(26) Botstein, D.; Waddell, C. H.; King, J. Mechanism of Head Assembly and DNA Encapsulation in Salmonella Phage-P22 0.1. Genes, Proteins, Structures and DNA Maturation. *J. Mol. Biol.* **1973**, *80*, 669−695.
(27) Lucon, J.; Qazi, S.; Uchida, M.; Bedwell, G. J.; LaFrance, B.; Prevelige, P. E.; Douglas, T. Use of the Interior Cavity of the P22 Capsid for Site-Specific Initiation of Atom-Transfer Radical Polymerization with High-Density Cargo Loading. *Nat. Chem.* **2012**, *4*, 781−788.
(28) Uchida, M.; Morris, D. S.; Kang, S.; Jolley, C. C.; Lucon, J.; Liepold, L. O.; LaFrance, B.; Prevelige, P. E.; Douglas, T. Site-Directed Coordination Chemistry with P22 Virus-Like Particles. *Langmuir* **2012**, *28*, 1998−2006.
(29) O'Neil, A.; Reichhardt, C.; Johnson, B.; Prevelige, P. E.; Douglas, T. Genetically Programmed *in Vivo* Packaging of Protein Cargo and Its Controlled Release from Bacteriophage P22. *Angew. Chem., Int. Ed.* **2011**, *50*, 7425−7428.
(30) Patterson, D. P.; Prevelige, P. E.; Douglas, T. Nanoreactors by Programmed Enzyme Encapsulation inside the Capsid of the Bacteriophage P22. *ACS Nano* **2012**, *6*, 5000−5009.
(31) Patterson, D. P.; Schwarz, B.; Waters, R. S.; Gedeon, T.; Douglas, T. Encapsulation of an Enzyme Cascade within the Bacteriophage P22 Virus-Like Particle. *ACS Chem. Biol.* **2014**, *9*, 359−365.
(32) Patterson, D. P.; McCoy, K.; Fijen, C.; Douglas, T. Constructing Catalytic Antimicrobial Nanoparticles by Encapsulation of Hydrogen Peroxide Producing Enzyme inside the P22 Vlp. *J. Mater. Chem. B* **2014**, *2*, 5948−5951.
(33) Qazi, S.; Miettinen, H. M.; Wilkinson, R. A.; McCoy, K.; Douglas, T.; Wiedenheft, B. Programmed Self-Assembly of an Active P22-Cas9 Nanocarrier System. *Mol. Pharmaceutics* **2016**, *13*, 1191−1196.
(34) Kang, S.; Uchida, M.; O'Neil, A.; Li, R.; Prevelige, P. E.; Douglas, T. Implementation of P22 Viral Capsids as Nanoplatforms. *Biomacromolecules* **2010**, *11*, 2804−2809.
(35) Parent, K. N.; Khayat, R.; Tu, L. H.; Suhanovsky, M. M.; Cortines, J. R.; Teschke, C. M.; Johnson, J. E.; Baker, T. S. P22 Coat Protein Structures Reveal a Novel Mechanism for Capsid Maturation: Stability without Auxiliary Proteins or Chemical Crosslinks. *Structure* **2010**, *18*, 390−401.
(36) Teschke, C. M.; McGough, A.; Thuman-Commike, P. A. Penton Release from P22 Heat-Expanded Capsids Suggests Importance of Stabilizing Penton-Hexon Interactions During Capsid Maturation. *Biophys. J.* **2003**, *84*, 2585−2592.
(37) Servid, A.; Jordan, P.; O'Neil, A.; Prevelige, P.; Douglas, T. Location of the Bacteriophage P22 Coat Protein C-Terminus Provides Opportunities for the Design of Capsid-Based Materials. *Biomacromolecules* **2013**, *14*, 2989−2995.
(38) Uchida, M.; McCoy, K.; Fukuto, M.; Yang, L.; Yoshimura, H.; Miettinen, H. M.; LaFrance, B.; Patterson, D.; Schwarz, B.; Karty, J. A.; Prevelige, P. E.; Lee, B.; Douglas, T. Modular Self-Assembly of Protein Cage Lattices for Multistep Catalysis. *ACS Nano* **2018**, *12*, 942−953.
(39) Tang, L.; Gilcrease, E. B.; Casjens, S. R.; Johnson, J. E. Highly Discriminatory Binding of Capsid-Cementing Proteins in Bacteriophage L. *Structure* **2006**, *14*, 837−845.
(40) Parent, K. N.; Deedas, C. T.; Egelman, E. H.; Casjens, S. R.; Baker, T. S.; Teschke, C. M. Stepwise Molecular Display Utilizing Icosahedral and Helical Complexes of Phage Coat and Decoration Proteins in the Development of Robust Nanoscale Display Vehicles. *Biomaterials* **2012**, *33*, 5628−5637.
(41) Llauro, A.; Schwarz, B.; Koliyatt, R.; de Pablo, P. J.; Douglas, T. Tuning Viral Capsid Nanoparticle Stability with Symmetrical Morphogenesis. *ACS Nano* **2016**, *10*, 8465−8473.
(42) Schwarz, B.; Madden, P.; Avera, J.; Gordon, B.; Larson, K.; Miettinen, H. M.; Uchida, M.; LaFrance, B.; Basu, G.; Rynda-Apple, A.; Douglas, T. Symmetry Controlled, Genetic Presentation of Bioactive Proteins on the P22 Virus-Like Particle Using an External Decoration Protein. *ACS Nano* **2015**, *9*, 9134−9147.
(43) Uchida, M.; LaFrance, B.; Broomell, C. C.; Prevelige, P. E.; Douglas, T. Higher Order Assembly of Virus-Like Particles (Vlps) Mediated by Multi-Valent Protein Linkers. *Small* **2015**, *11*, 1562−1570.
(44) Liljestrom, V.; Seitsonen, J.; Kostiainen, M. A. Electrostatic Self-Assembly of Soft Matter Nanoparticle Cocrystals with Tunable Lattice Parameters. *ACS Nano* **2015**, *9*, 11278−11285.
(45) Valimaki, S.; Mikkila, J.; Liljestrom, V.; Rosilo, H.; Ora, A.; Kostiainen, M. A. Hierarchically Ordered Supramolecular Protein-Polymer Composites with Thermoresponsive Properties. *Int. J. Mol. Sci.* **2015**, *16*, 10201−10213.
(46) Macfarlane, R. J.; Lee, B.; Jones, M. R.; Harris, N.; Schatz, G. C.; Mirkin, C. A. Nanoparticle Superlattice Engineering with DNA. *Science* **2011**, *334*, 204−208.
(47) Chang, J.; Weigele, P.; King, J.; Chiu, W.; Jiang, W. Cryo-Em Asymmetric Reconstruction of Bacteriophage P22 Reveals Organization of Its DNA Packaging and Infecting Machinery. *Structure* **2006**, *14*, 1073−1082.
(48) Patterson, D. P.; Schwarz, B.; El-Boubbou, K.; van der Oost, J.; Prevelige, P. E.; Douglas, T. Virus-Like Particle Nanoreactors: Programmed Encapsulation of the Thermostable Celb Glycosidase inside the P22 Capsid. *Soft Matter* **2012**, *8*, 10158−10166.
(49) Langford, J. I.; Wilson, A. J. C. Scherrer after 60 Years - Survey and Some New Results in Determination of Crystallite Size. *J. Appl. Crystallogr.* **1978**, *11*, 102−113.
(50) Fan, W.; Ogura, M.; Sankar, G.; Okubo, T. *In Situ* Small-Angle and Wide-Angle X-Ray Scattering Investigation on Nucleation and Crystal Growth of Nanosized Zeolite A. *Chem. Mater.* **2007**, *19*, 1906−1917.
(51) Warren, B. E. X-Ray Diffraction in Random Layer Lattices. *Phys. Rev.* **1941**, *59*, 693−698.

DOI: 10.1021/acsnano.8b00528
ACS Nano 2018, 12, 3541−3550